Earthq Eng & Eng Vib (2015) 14: 385-398 **DOI**:10.1007/s11803-015-0031-4

Three-dimensional simulations of strong ground motion in the Shidian basin based upon the spectral-element method

Liu Qifang[1, 2†], Yu Yanyan[1, 2‡] and Zhang Xubin[1, 2‡]

1. *Institute of Engineering Mechanics, China Earthquake Administration, Harbin 150080, China*

2. *Key Laboratory of Earthquake Engineering and Engineering Vibration, China Earthquake Administration, Harbin 150080, China*

Abstract: The strong motion of a small long and narrow basin caused by a moderate scenario earthquake is simulated by using the spectral-element method and the parallel computing technique. A total of five different geometrical profiles within the basin are used to analyze the generation and propagation of surface waves and their relation to the basin structures in both the time and frequency domain. The amplification effects are analyzed by the distribution of peak ground velocity (PGV) and cumulative kinetic energy (Ek) in the basin. The results show that in the 3D basin, the excitation of the fundamental and higher surface wave modes are similar to that of the 2D model. Small bowls in the basin have great influence on the amplification and distribution of strong ground motion, due to their lateral resonances when the wavelengths of the lateral surface waves are comparable to the size of the bowls. Obvious basin edge effects can be seen at the basin edge closer to the source for constructive interference between direct body waves and the basin-induced surface waves. The Ek distribution maps show very large values in small bowls and some corners in the basin due to the interference of waves propagating in different directions. A high impedance contrast model can excite more surface wave modes, resulting in longer shaking durations as well as more complex seismograms and PGV and Ek distributions.

Keywords: 3D Shidian basin; spectral element method; basin-edge effect; lateral resonance; surface wave; peak ground velocity; cumulative kinetic energy

1 Introduction

Sedimentary basins can significantly amplify the ground motion within certain frequency bands and contribute to loss of life and damage to a structure (Liao, 2011; Paudyal *et al*., 2012; Zhang *et al*., 2015). During some earthquakes, it was observed that damage in the basins is more severe than near the epicenter. For example, the 1985 Michoacan earthquake caused significant damage in Mexico City, although the city lies more than 400 km from the epicenter (Anderson *et al*., 1986). Similarly, the 2002 Hualien, Taiwan, offshore earthquake (M_L 6.8) caused minor damage near the epicenter but significant damage in the Taipei basin, which is located about 110 km from the epicenter (Chen, 2003).

Numerical simulations, such as the Aki-Larner method (Bard and Bouchon, 1980a, 1980b; Horike *et al*., 1990), the finite element method (Bao *et al*., 1998), the finite difference method (Graves *et al*., 1998; Olsen and Schuster, 1995; Olsen, 2000; Lee *et al*., 2008a), the boundary element method (Semblat *et al*., 2002; Lee, 2013), the spectral element method (Komatitsch *et al*., 2004; Delavaud *et al*., 2006; Lee *et al*., 2008b; Pilz *et al*., 2011), and the mixed method (Kim *et al*., 2003) are usually used to discover the cause of the basin amplification effect. These studies have shown some characteristics of the ground motions in basin, including the trapping of seismic wave energy of specific frequencies because of high velocity contrast between the sediments and the underlying bedrock, the generation of surface waves at the basin edges resulting from the wave reflections and mode conversions, and the long duration of strong motion because of slow attenuation and back-and-forth propagation of surface waves in the basin, etc. Moreover, at the basin edge, ground motions may be amplified because of constructive interference between direct body waves and basin-induced surface waves, which is also called the basin-edge effect (Kawase, 1996; Pitarka *et al*., 1998).

There are many small sedimentary basins in southwest China, where seismic disasters have been significantly greater than that of the surrounding areas during historical earthquakes. A typical example is the long and narrow Shidian basin, which is located in the southwest region of Yunnan province with the largest width of about 4 km in the east-west direction and

---

Correspondence to: Liu Qifang, Institute of Engineering Mechanics, China Earthquake Administration, Harbin 150080, China
Tel: +86-451-86652622
E-mail: Qifang_liu@126.com

†Professor; ‡Master Student

Supported by: National Natural Science Foundation of China under Grant No. 51078337, No. 51108431 and No. 91315301

Received January 23, 2014; **Accepted** October 12, 2014

length of about 18 km in the north-south direction. The 1976 Longling earthquake (M_L 7.3), the 1988 Lancang-Gengma earthquake (M_L 7.6), and the 2001 Shidian earthquake (M_L 5.9) have caused abnormally high damage intensity in this basin, although the epicenters of these earthquakes are located tens to hundreds kilometers from the basin (see Fig. 1(a)). Figure 1(b) shows the isoseismal map of the Longling earthquake, where the Shidian basin is an obvious area of abnormal intensity, although it is located about 70 km from the epicenter.

To investigate the amplification effect within the Shidian basin, wave field simulations considering a moderate scenario earthquake based on a 3D basin model established in a previous study (Liu *et al.*, 2013) were carried out. The emphasis is on the generation and propagation of basin-induced surface waves, and the influence of basin geometry and impedance contrast on the basin-internal strong motions. The wave propagation snapshot, synthetic waveform, different surface wave modes, distribution of peak ground velocity (PGV) and cumulative kinetic energy (E_k) are used to analyze the characteristics of the basin strong motion in detail.

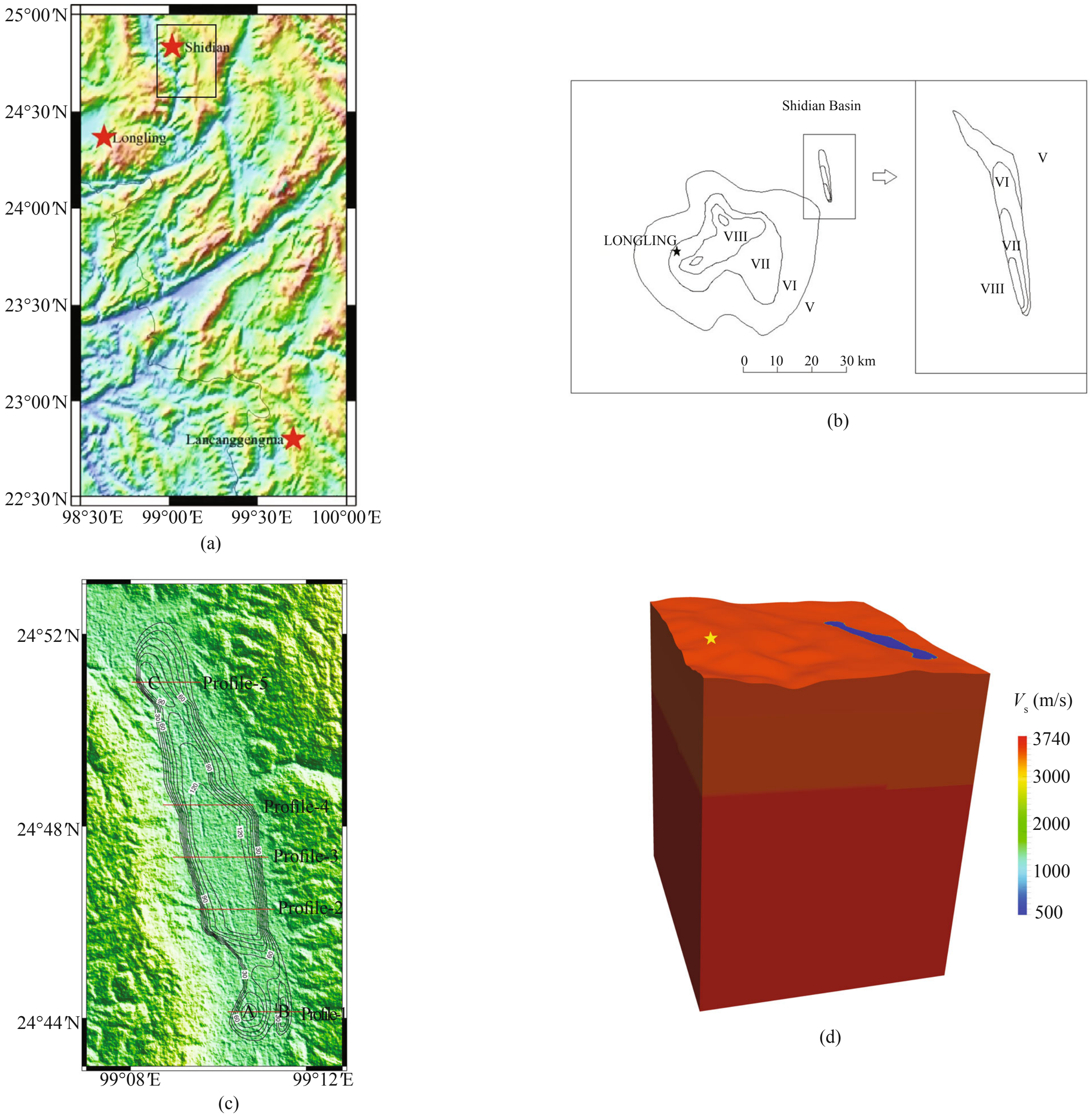

(a) (b) (c) (d)

Fig. 1 (a) Location of Shidian basin and some historical damage earthquakes. The boxcar depicts the calculation area; (b) The isoseismal map of Longling earthquake (M_L = 7.3, after Yuan *et al.*, 1992). The Shidian basin is a high abnormal intensity area; (c) Depth distributon of the sedmentary in Shidian basin where the red lines denote the profiles to be studied; and (d) The calculation model where the blue area indicates the Shidian basin and the yellow star denotes the scenario earthquake epicenter. Note that the scale of vertical direction is twice of the horizontal direction

2 Brief description of the Shidian basin model

Liu *et al.* (2013) has described a complex 3D basin model by using 24 boreholes drilling wells and other seismic geology data, and the basin basement is determined in this model. The basement depth isolines and five profiles selected to study the basin amplification behavior are shown in Fig. 1(c). Some characteristics can be observed: (1) two scarps with rapidly changing sediment thickness are located near Profiles 2 and 4, and a relatively flat layer with the largest depth of about 120 m is located in the central part of the basin between these two scarps; (2) three relatively local deeper parts (denoted by A, B, and C in Fig. 1(c), and referred to as Bowls A, B and C of the basin hereafter) lie in the basin with a maximum depth of about 110 m for Bowl C and 80 m for Bowls A and B; (3) from the isoline of the basement depth, it is found that the dipping angle of the west basin edge is generally larger than that of the east.

The P- and S- wave velocities in the basin are taken as constant values of 1100 and 500 m/s, respectively. Note that it is not the real basin velocity structure since there is not enough data to determine it. Outside the basin, the 1-D velocity structure of the crust in the Sichuan-Yunnan region of China (Wang *et al.*, 2002) is adopted. A constant value of $Q_u = 30$ is used for the sediments. The velocity structure parameters are listed in Table 1. This model is referred to as the "basic model" in the following discussion. Although the sediment parameters are somewhat unusual in nature, such a high impedance contrast model facilitates our study of the main characteristics of the basin response.

Table 1 Velocity structure of the calculation model

Depth (km)	V_p (km/s)	V_s (km/s)	Density (g/cm^3)	Q_u
Within basin	1.1	0.5	1.8	30
1	5.89	3.45	2.6	600
10	5.88	3.43	2.6	800
28	6.45	3.74	2.75	900

3 Earthquake scenario

A double-couple point source with strike 0°, dip 90°, rake 0° and focal depth of 5.0 km located at (3.966 km, 14.0 km) is taken as scenario earthquake in this study. The epicenter is located about 15 km to the west basin edge (Fig .1(d)). The static moment is assumed to be 3.21×10^{14} kN·m. A Gaussian source time function is used with a duration of 0.4 s that constrains the response frequency between 0.05 Hz to 3.0 Hz. Figure 2 shows the source time function and its Fourier spectra.

4 Spectral-element scheme

Wave motions are simulated by using the spectral-element method (Komatitsch *et al.*, 2004) and parallel computing technique. The model covers 24 km in the east direction and 30 km in the north direction at the surface and extends to 28 km in depth. At all sides and bottom of the computational model, paraxial boundary condition (Clayton and Engquist, 1977) are applied. Realistic three-dimensional surface topography is incorporated in the simulations. The grid size inside the basin is about 60 m horizontally and 30 m vertically. A small vertical grid size is chosen in the basin to better describe the boundary between sediments and bedrock, and coarser mesh is used outside the basin to reduce the computational cost. The mesh contains 777,254 spectral elements that are decomposed into 76 slices for parallel computing. Since a polynomial degree $N = 4$ is used in SEM to simulate the wavefield, each spectral element contains $(N+1)^3 = 125$ Gauss–Lobatto–Legendre (GLL) points (Komatitsch *et al.*, 2004), the mesh includes 51.5 million grid points. Based on the rule-of-thumb that roughly five points per minimum wavelength for the SEM, the maximum resolved frequency is about 3.0 Hz

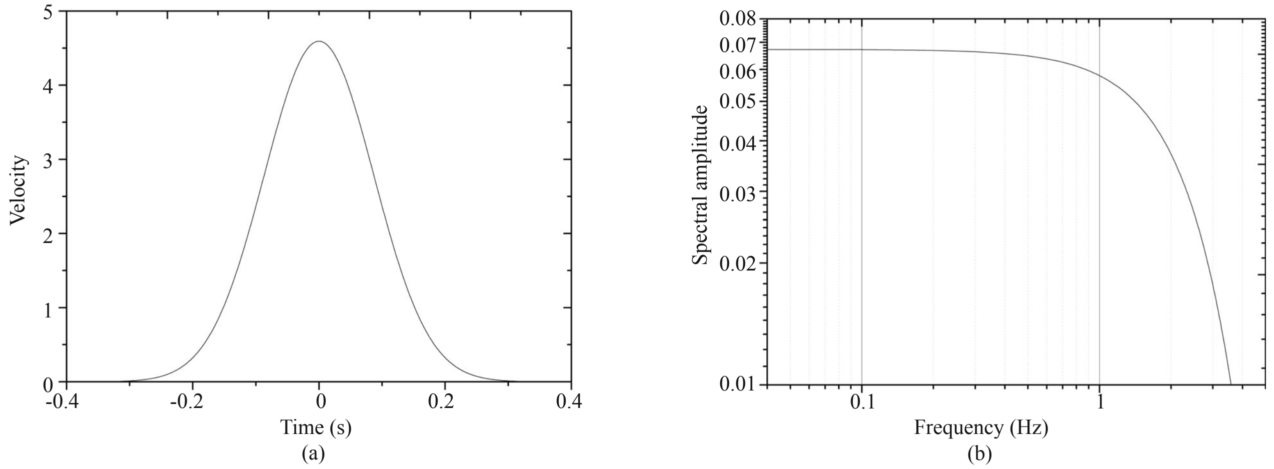

(a) (b)

Fig. 2 (a) Gaussian source-time function used in the simulations with a duration of 0.4 s; (b) Spectral amplitude of the source

for the current Shidian basin model. The simulations are performed on a DELL OPTIPLEX cluster (17 nodes, 76 processors) with a time step of 0. 35 ms, and the total computing time is about 15 hours for a 30 s simulation.

5 Simulation results

In this section, the generation and propagation of basin-induced surface waves are investigated in detail by ground velocity snapshots and synthetic seismograms along profiles in both a space-time and wavenumber-frequency domain, and the amplification behaviors are analyzed by the distribution of PGV and E_k.

5.1 Wave-field snapshots

The snapshots of vertical component velocity at the surface are shown in Fig. 3. Between 2.8 s and 3.5 s, the P waves travel through the basin. Within this time, the vibrations in the basin are relatively weak, and no clear surface waves can be observed. When S waves enter the basin (about 5.0 s), the amplitudes in the basin become obviously larger and are much larger than that outside the basin due to the low wave-speed sediments.

In addition, the S-wave fronts are clearly delayed and distorted inside the basin because of the low velocity in the basin. At about 6.3 s, the S waves roughly pass through the basin, while most of the energy is trapped in it. Almost at the same time, large-amplitude surface waves (Rayleigh waves) propagate after the S wave can be observed. Surface waves are mainly generated by the mode conversions of the S waves at the basin edge, and parts of them are reflected back into the basin when they reach the opposite edge. This phenomenon is particularly clear at a time 7.0 s and 8.4 s. At about 14 s, the ground motions in the basin attenuate to a relatively small value. Note that both the east-west and north-south propagating surface waves exist in the basin at the same time, which further lengthens the ground shaking time within the basin.

5.2 Synthetic seismograms

To study the correlations between basin amplification behavior and its geometry, synthetic velocity seismograms along profiles 1 to 5 in a time-space and frequency-wavenumber domain are investigated in detail. As shown in Fig. 1(b), Profiles 1 and 5 transect the local bowls, Profile 3 just lies in the east direction

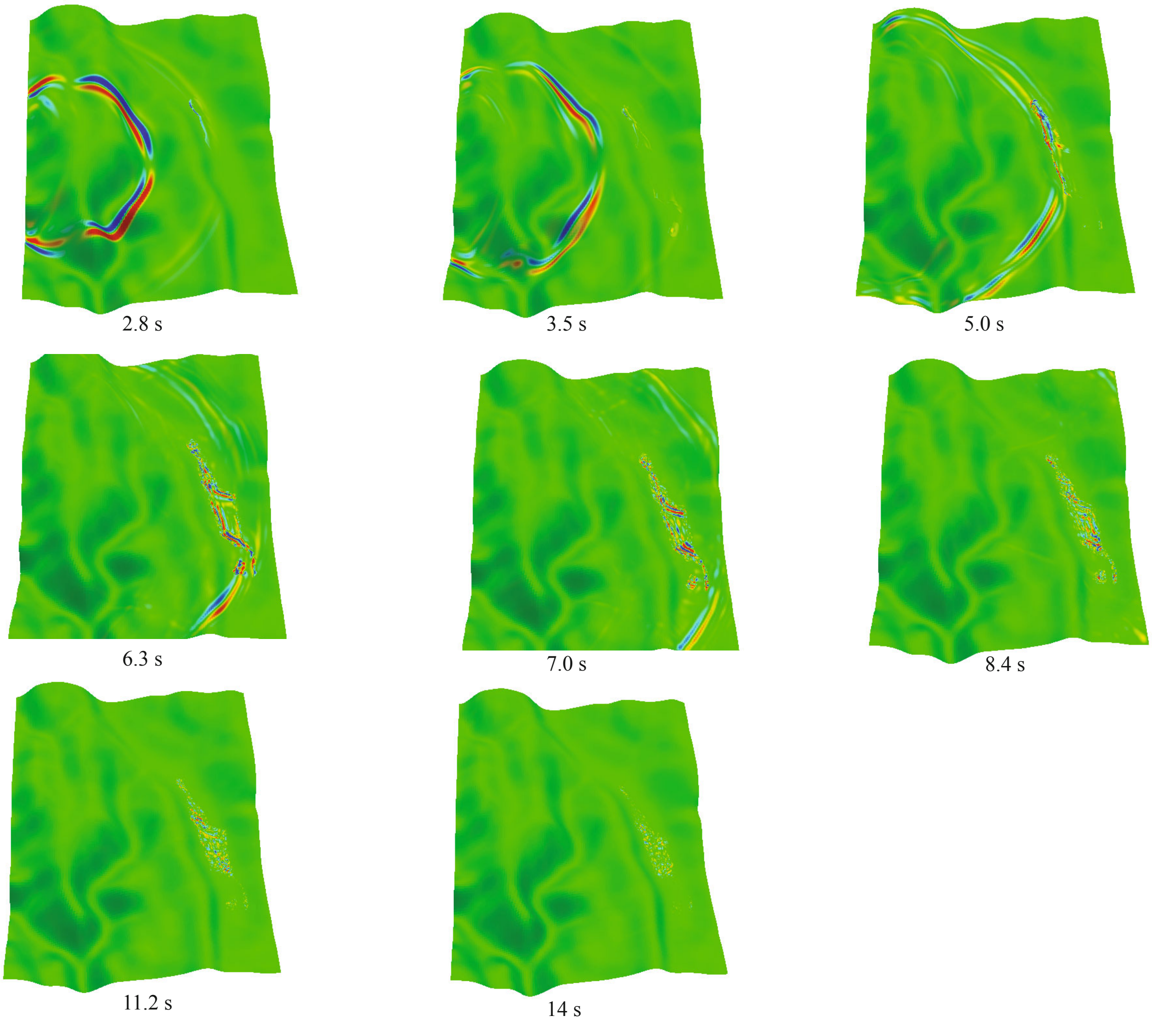

2.8 s 3.5 s 5.0 s

6.3 s 7.0 s 8.4 s

11.2 s 14 s

Fig. 3 Snapshots of the ground vertical component velocity of the basic model. Red / blue shading denotes positive / negative particle velocity

to the epicenter, and Profiles 2 and 4 are located in the area near scarps. Figure 4 shows the synthetic velocity waveforms along these profiles. The seismograms are normalized by the maximum PGV value within the basin of the three components. Figure 6 shows the frequency domain response of Profiles 1 to 5 for the east and north component. The negative and positive wavenumbers denote the eastwards and westwards propagating waves, respectively, and the amplitudes in Fig. 6 are normalized by the maximum spectrum value of all the profiles.

The most interesting feature of the time histories of Profile 1 concerns the in-phase motions of the Bowl A and B with large amplitudes, and the frequency domain responses (Fig. 6, Profile 1) show that the large amplitudes stay around stationary frequencies of about 2.4 Hz and 1.75 Hz for varying wavenumbers at the east and north component, respectively, indicating that the corresponding group velocities are approximately equal to zero. In other words, resonances may occur in the two bowls. In addition, it is noted that the amplitudes of the Bowl A are obviously larger than that of the Bowl B, though their soil depths are approximate. An interpretation for this phenomenon may be that, as the Bowl A is circle-shaped with similar width and length of 360 m and 420 m (Fig. 1(c)), respectively, surface waves from different directions in the Bowl A may meet at its center due to the circle shape. The lateral interferences between these surface waves may set up multi-dimensional lateral resonance. However, the Bowl B is long and narrow with about 300 m width and 1000

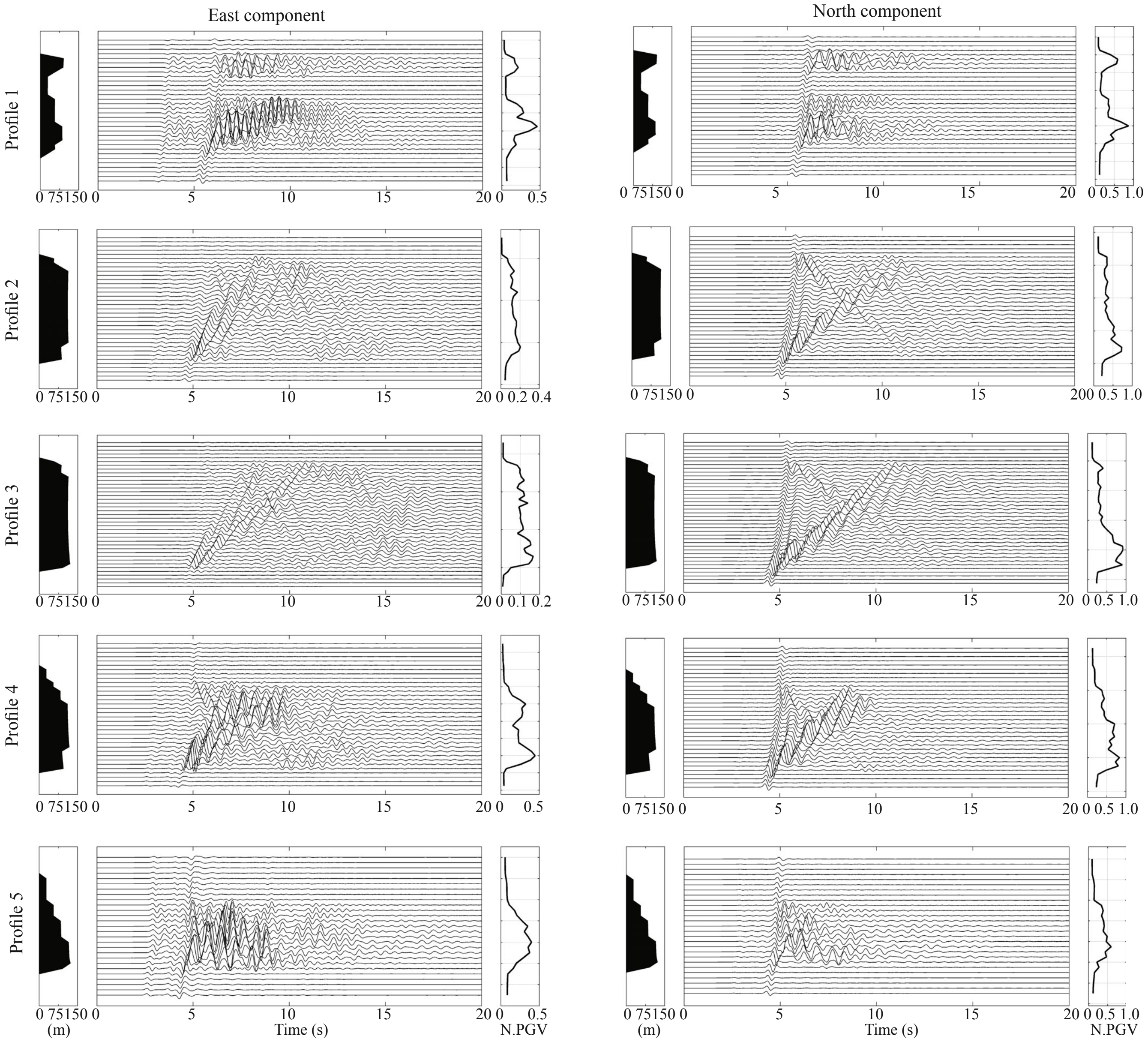

Fig. 4 Synthetic velocity seismograms of the east and north component along Profiles 1 to 5. Corresponding sediment thicknesses and normalized PGV values are also shown in each subfigure; the bottom and top of each subfigure denotes the west and east direction of the basin, respectively

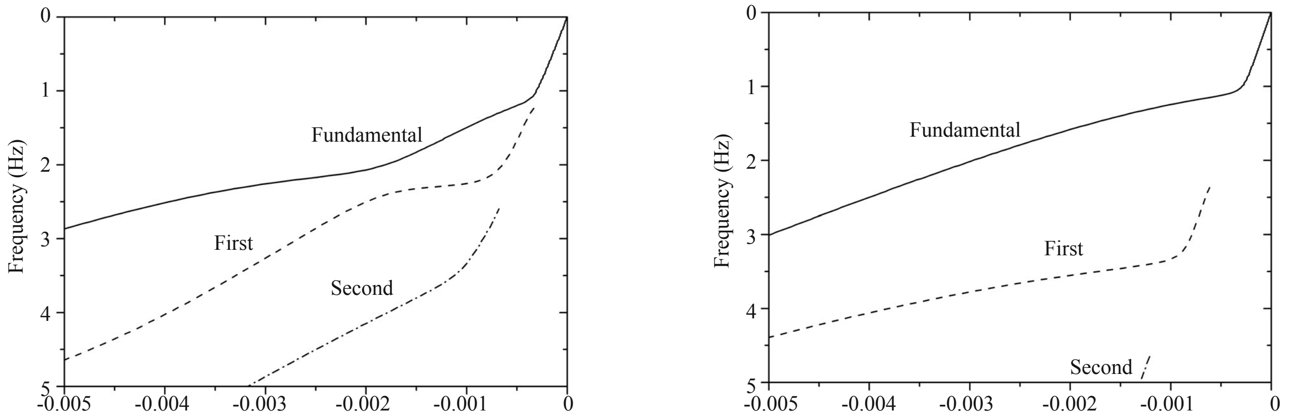

(a) Rayleigh wave (b) Love wave

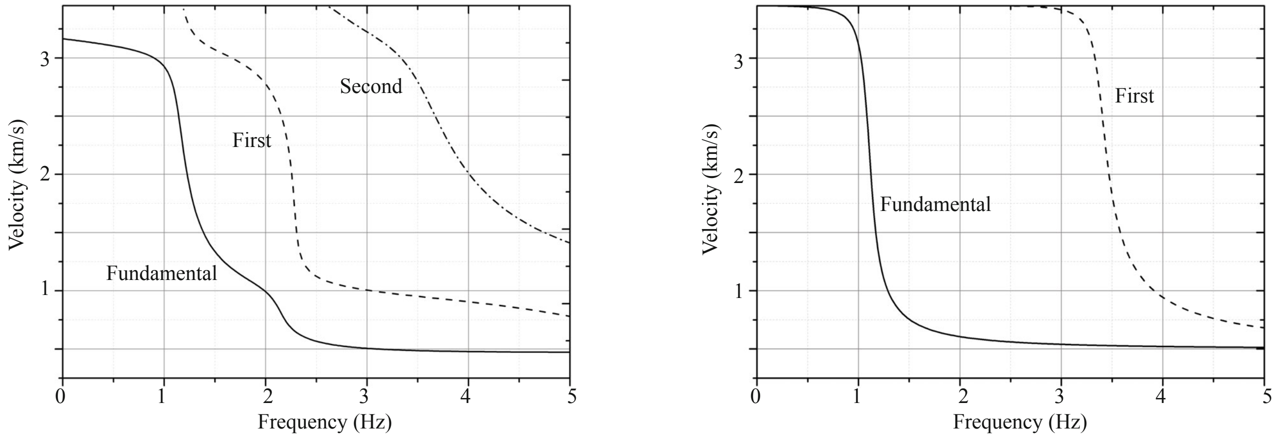

(c) Rayleigh wave (d) Love wave

Fig. 5 Theoretical dispersion curves of Rayleigh and Love waves for the equivalent plane layer of Profile 3. (a) Horizontal wavenumber versus frequency for Rayleigh wave; (b) Same as (a), but for Love wave; (c) Phase velocity versus frequency for Rayleigh wave; (d) Same as (c), but for Love wave

m length, so the east-west and north-south propagating surface waves interfere asynchronously because of its very different width and length. As a result, the one-dimensional lateral resonance causes smaller amplitudes compared with the multi-directional interference case.

The horizontal resonance phenomenon can also be observed in the Bowl C of Profile 5. Since its width is about 600 m in the east direction, which is larger than that of the Bowls A and B on Profile 1, the resonance frequency of the Bowl C consequently becomes lower, which can be observed in both the time and frequency domains. In addition, due to the asynchronous lateral interference of the east-west and north-south propagating surface waves because of its long and narrow shape, the resonance amplitudes of Bowl C are smaller compared with that of Bowl A, though their sediment thickness is similar.

Seismograms of Profiles 2, 3, and 4 are dominated by large amplitude surface waves generated at the basin edge. For the radiation pattern of the current point source, since Profiles 2 to 4 are located in the epicenter azimuth less than 10°, the amplitude of the incident wave is quite large for the S-wave and very small for the P-wave, and most of the S-wave is on the north component. Since the SV wave is mainly on the east and vertical component and the SH wave is on the north component, the surface waves on the east and north component seismograms of Profiles 2, 3, and 4 are mainly the Rayleigh and Love waves, respectively, with amplitudes of the Love wave larger than the Rayleigh wave. Consequently, amplitudes of the north component on these profiles are much larger than that of the east and vertical component (not shown here) for all these profiles.

For the east component of Profile 3, surface waves generated at the western basin edge are divided into the fundamental and the first higher mode, with phase velocities of 0.65 km/s and 1.25 km/s (Fig. 4, Profile 3), respectively. In addition, large amplitude scattered waves arrive almost simultaneously after the direct Rayleigh waves, which are probably the surface waves propagating from the north scarp near Profile 3. This disturbance significantly prolongs the shaking time around this profile. For the north component, an obvious fundamental Love wave mode can be seen at both basin edges with phase velocity about 0.6 km/s (Fig. 4, Profile 3). These velocity values agree well with the theoretical dispersion curve of a flat layer with thickness equals to the maximum depth of Profile 3, as shown in Fig. 5. Similar to Bard and Bouchon (1980a), this flat layer is referred to as the "equivalent plane layer" in the

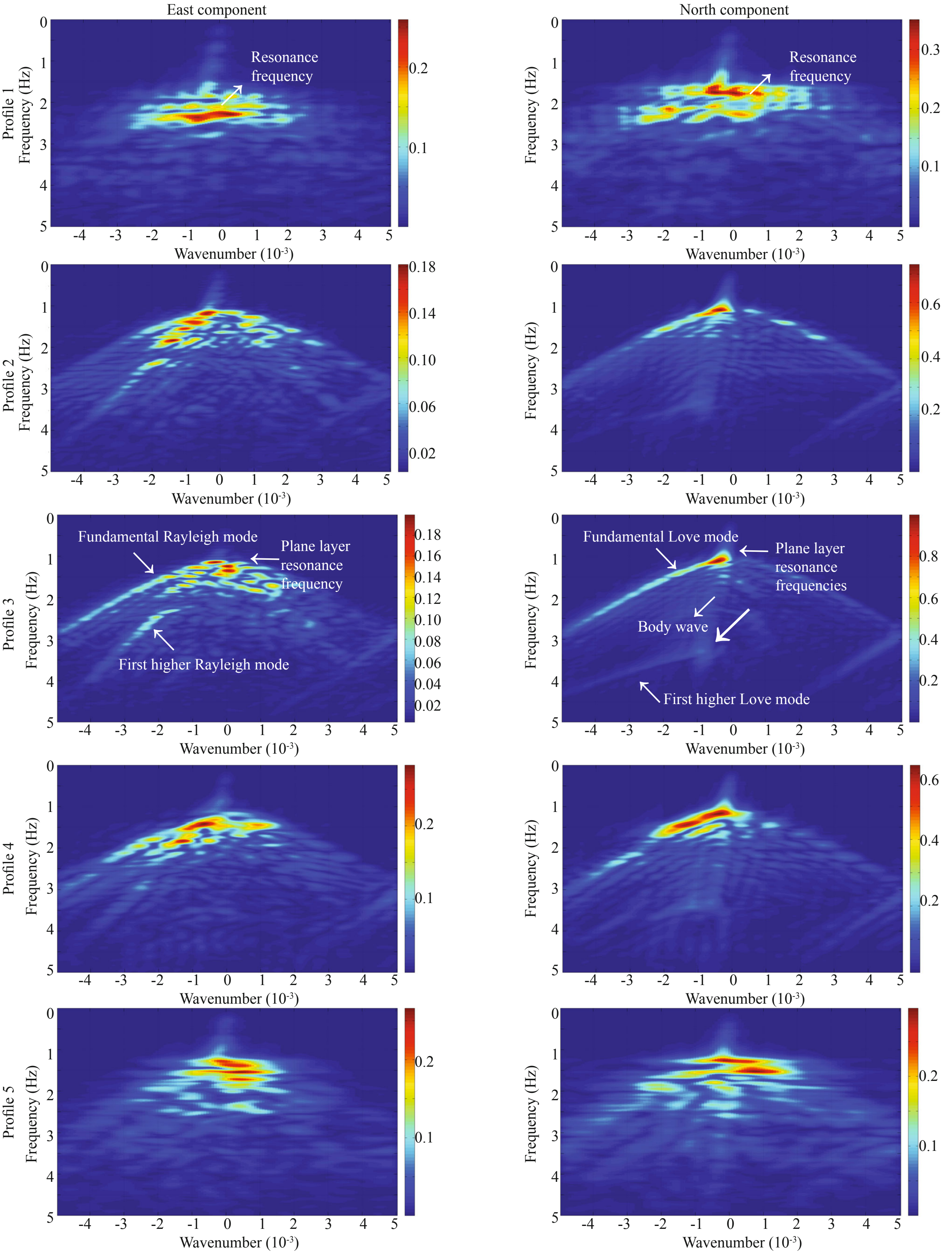

Fig. 6 Frequency domain responses of Profiles 1 to 5 for the east and north component. The amplitudes of each (f, k) component that is normalized by the maximum value of all the five profiles are shown on the right of each subfigure

following discussion.

Note that amplitudes of the fundamental and the first higher Rayleigh modes are different on the east components of Profiles 2 and 3. On Profile 2, from both the time and frequency domains, it is found that the amplitudes of the first higher Rayleigh mode are larger than that of the fundamental mode. However, on Profile 3, the amplitudes of the fundamental and the first higher Rayleigh modes are similar.

On Profile 4, amplitudes of the east component waveforms are much larger and more complex than that of Profiles 2 and 3, though their basin depths are almost the same, which may be caused by the constructive interference of the east and south propagating surface waves and the scattered waves by the irregular basement. The frequency domain responses (see Fig. 6) show that the predominant features of seismic motions along this profile are also the first two Rayleigh modes for the east component, and the fundamental Love mode for the north component.

For both the east and north components of Profiles 2 to 4, the surface waves at the western basin edge are generally stronger than that of the eastern edge, which can be seen from the PGVs along these profiles (Fig. 4) and the frequency domain responses. This may be due to the steeper western basin edge and the eastward incidence direction. In this case, the incident energy towards the west basin edge is higher than that of the east edge.

The basic features of frequency domain responses of Profiles 2 to 4 (Fig. 6) are similar for their approximate soil depths and flat basements. As pointed out by Haskell (1960), for a wave vertically incident on a plane layer with a shear wave velocity β_1 and a thickness h, the vertical resonance frequencies are

$$f_n = (2n+1)\frac{\beta_1}{4h} \tag{1}$$

Bard and Bouchon (1980a, b) studied the development of different Love and Rayleigh modes under SH and SV wave incident cases for a 2D basin model, where it was found that the Love modes develop as soon as the frequency exceeds the corresponding plane layer resonance frequency, and the first two and the second higher Rayleigh modes are excited as soon as the fundamental S-wave resonance frequency ($\beta_1/4h$) and the second resonance frequency ($3\beta_1/4h$) is exceeded.

It is observed from the frequency domain responses of Profiles 2 to 4 (Fig. 6) that besides the fundamental resonance frequency on the east component and the first two resonance frequencies on the north component, two main branches starting from them can be distinguished, which correspond exactly to the dispersion laws *k* (*f*) of the fundamental and the first higher Rayleigh and Love modes in a flat layer with the same thickness (Figs. 5(a), (b)). On the east component (Fig. 6), the first two Rayleigh modes are simultaneously excited when the frequency exceeds the fundamental S-wave vertical resonance frequency ($f_v = \beta_1/4h$, about 1.1 Hz) of the equivalent plane layer. However, the strength of the first two Rayleigh modes varies for different profiles. For instance, the first higher Rayleigh mode demonstrates larger amplitudes than that of the fundamental mode on Profiles 2 and 4. However, they are comparable on Profile 3.

For the north component of Profiles 2 to 4, it is shown that the fundamental and the first higher Love modes are excited as soon as the frequencies exceed the first two vertical resonance frequencies of the corresponding plane layers (about 1.1 and 3.3 Hz, respectively). The Love wave energy is mainly composed of the fundamental mode with larger amplitudes for the eastwards propagating surface waves and the largest amplitudes around the frequency f_v. The first higher Love mode only contains the eastwards propagating waves with relatively insignificant shaking intensity. In addition to the surface waves, body waves can also be observed in Fig. 6, which correspond to the branches starting from the origin and characterized by constant phase velocity roughly equals to the shear wave velocity of the bedrock. Here the phase velocity is defined as the slope between the origin and the wave component (*f, k*). As shown in the diagrams, shaking amplitudes of the north component body waves on Profile 3 are comparable to that of the first higher Love mode but are much smaller than the fundamental mode.

The second and higher surface wave modes are not presented in Fig. 6 since the incident waves do not excess their excitation frequencies. It is expected that these higher modes will appear if the incident frequency is high enough.

5.3 Distribution of PGV and cumulative kinetic energy

The distributions of PGV and cumulative kinetic energy are used to analyze the influence of the 3D Shidian basin model on ground motions, and these two parameters are usually related to the basin geometry as studied by some researchers (Olsen and Schuster, 1995; Lee *et al.*, 2008a). The cumulative kinetic energy per unit volume is defined as the sum of the square of the velocity amplitudes of all three components in the seismogram in time, multiplying the density ρ, that is,

$$E_{\mathrm{k}}(x,y) = \frac{1}{2}\rho(x,y)\sum_{k=1}^{3}\int \dot{u}_k^2(x,y,t)\mathrm{d}t \tag{2}$$

As shown in Fig. 7, the PGV distributions are obviously influenced by the source radiation pattern. As discussed above, along the cross section of y = 14 km (Profile 3), the SV waves show relatively small amplitudes on the east and vertical component, and SH waves possess the largest amplitudes on the north component, resulting in amplitudes of Love waves larger than that of Rayleigh waves. Thus, the PGV values along

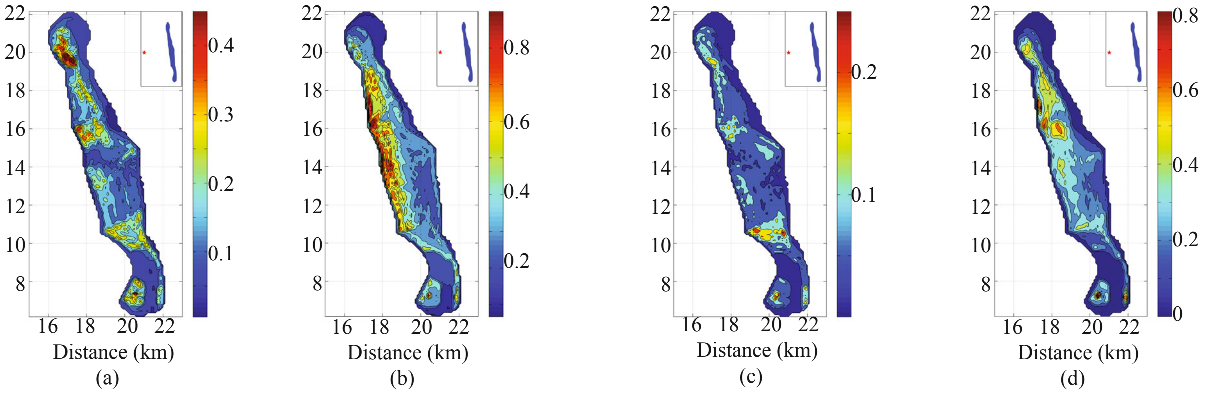

(a) (b) (c) (d)

Fig. 7 Distribution of PGV and E_k for the basic model. (a) PGV, east component; (b) PGV, north component; (c) PGV, vertical component; (d) E_k. The insert of each subfigure shows the location of the epicenter and the basin

Profile 3 are significantly large in the north component and quite small in east and vertical component.

The PGV distribution displays clear basin edge effect at the north component. Large amplitude ground motions are concentrated in a narrow belt zone near the western basin edge because of constructive interference between basin-induced surface waves and direct body waves. However, at the eastern edge, the basin edge effect is not apparent since the basin induced surface waves are relatively weak.

The PGV distribution shows rather large values at the Bowls A, B and C, and some corners between $y = 10$ to 16 km on the east and vertical component, where the amplitudes are about 3-5 times that at other areas with similar soil thickness. As discussed above, this may be caused by the trapping of energy within the bowls or the constructive interference between waves from different directions at the corner, which both lead to subsequent vibrations with considerably large amplitudes. The E_k distribution shows similar characteristics to that of the PGV of the north component, except some large values at the bowls and corner around (18 km, 16 km) of the basin.

6 Discussion

6.1 Effects of impedance contrast between sediment and bedrock

Shear wave impedance contrast between the basin and bedrock determines how much incident seismic energy can transmit at the sediment-bedrock interface, and thus affects the generation of basin-induced surface waves, which has been discussed in detail by Bard and Bouchon (1980a, b) for 2D basins. To analyze its influence on the ground motions of a 3D basin, three different models are considered: (1) high impedance contrast model with S-wave velocity in the basin of 200 m/s (Model 1), (2) the basic model (Model 2), and (3) low impedance contrast model with S-wave velocity in the basin of 1100 m/s (Model 3). For all these models, the other parameters remain unchanged.

An analysis on surface wave generation and propagation is performed first. Figure 8 shows the east and north component seismograms and normalized PGV along Profile 3 for the three tested models. As shown in Fig. 8, Model 1 displays the most complex time histories, since higher surface wave modes can be excited for its relatively low soil velocity.

For the east component, higher mode surface waves (Rayleigh wave) can be clearly observed for Models 1 and 2, whereas only the fundamental mode exists in Model 3 since the excitation frequency of the higher surface wave modes is much larger than the incident frequency band. From the comparison between north component seismograms of the three models, surface wave amplitudes of Model 1 and 2 are larger than that of the body waves, whereas the amplitudes of body and surface waves are comparable for Model 3.

As impedance contrast decreases, such as in Model 3, the surface waves become less apparent for the east component, and only the eastwards propagating Love waves exist for the north component. This is similar to the results of the 2D models of Bard and Bouchon (1980a). Moreover, north-south propagating surface waves on the east component become stronger for Model 3, which is particularly clear during 7–9 s.

To further examine the difference between the three tested models, the east and north component responses in the frequency-wavenumber domain are presented in Fig. 9.

The responses of profile 3 for the three tested models in the frequency domain are discussed first (Fig. 9(a), bottom; Fig. 9(b), bottom). For Model 1, since its shear velocity is 200 m/s, the first three vertical resonance frequencies of the equivalent plane layer of Profile 3 are about 0.45 Hz, 1.35 Hz, and 2.25 Hz. On the east component (Fig. 9(a), bottom left), the fundamental and the first higher Rayleigh modes are excited simultaneously as soon as the frequency exceeds the fundamental plane layer resonance frequency (about

0.45 Hz), and the second higher Rayleigh mode develops when the frequency exceeds about 1.35 Hz. On the north component (Fig. 9(a), bottom right), the fundamental, the first higher, and the second higher Love modes are excited as soon as the frequency exceeds about 0.45 Hz, 1.35 Hz, and 2.25 Hz, respectively. For Model 2, the shear

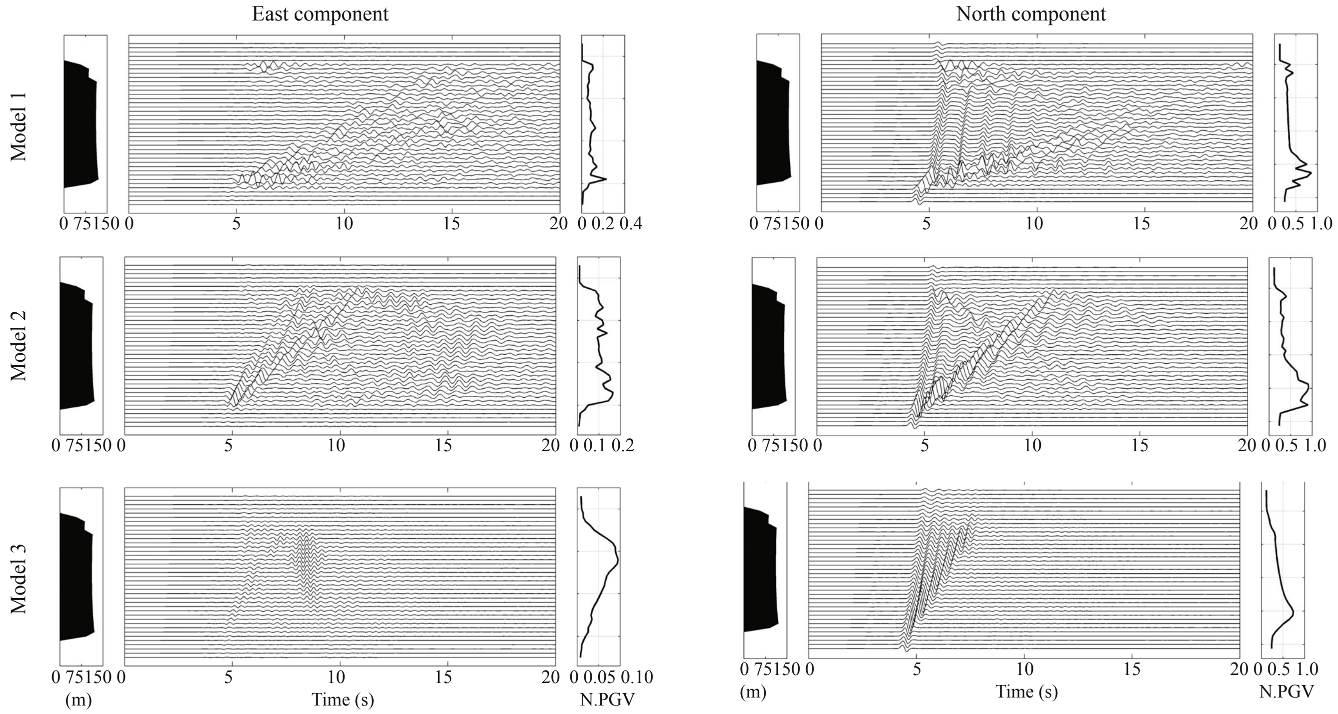

Fig. 8 East and north component velocity seismograms of Profile 3 for the three tested models, the bottom and top of each subfigure denotes the west and east direction of the basin, respectively

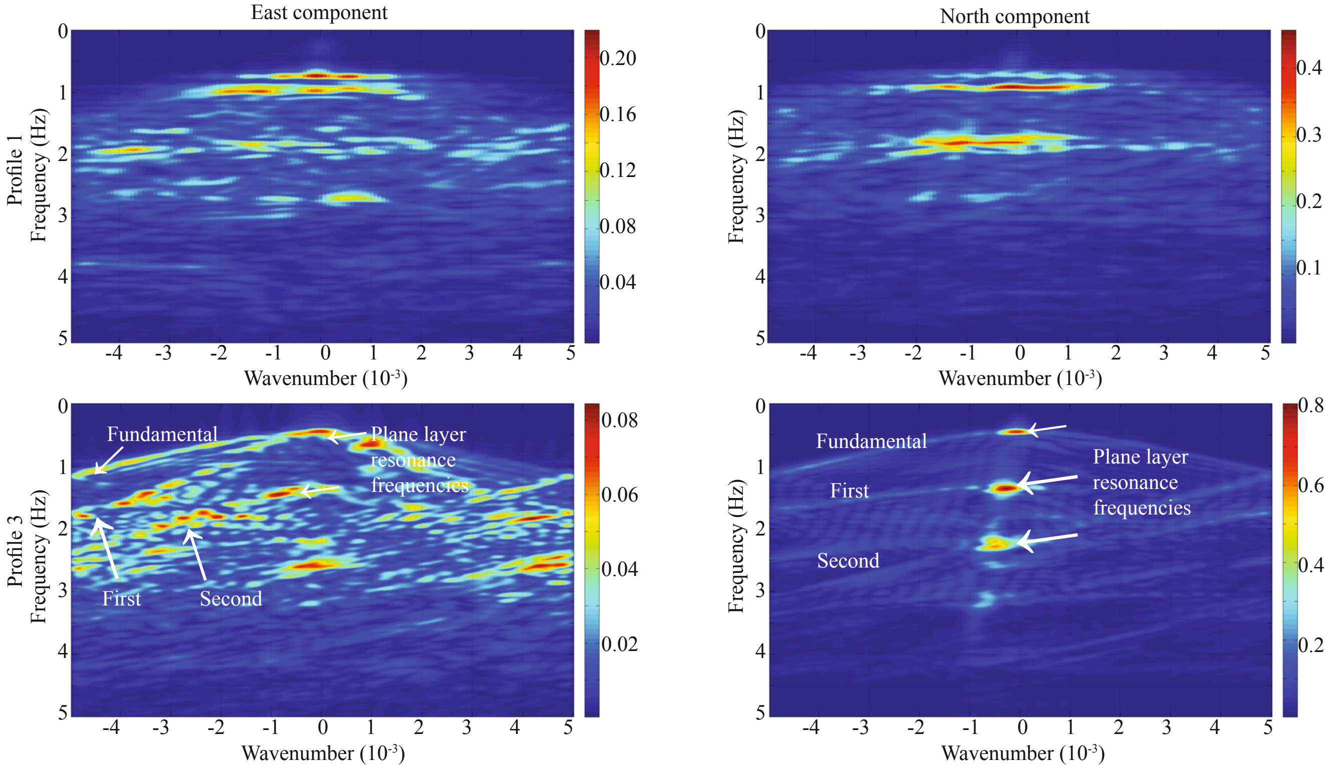

(a) Model 1

Fig. 9 East and north component responses of Profiles 1 and 3 in the frequency domain for (a) sediment velocity 200 m/s (Model 1) and (b) sediment velocity 1100 m/s (Model 3)

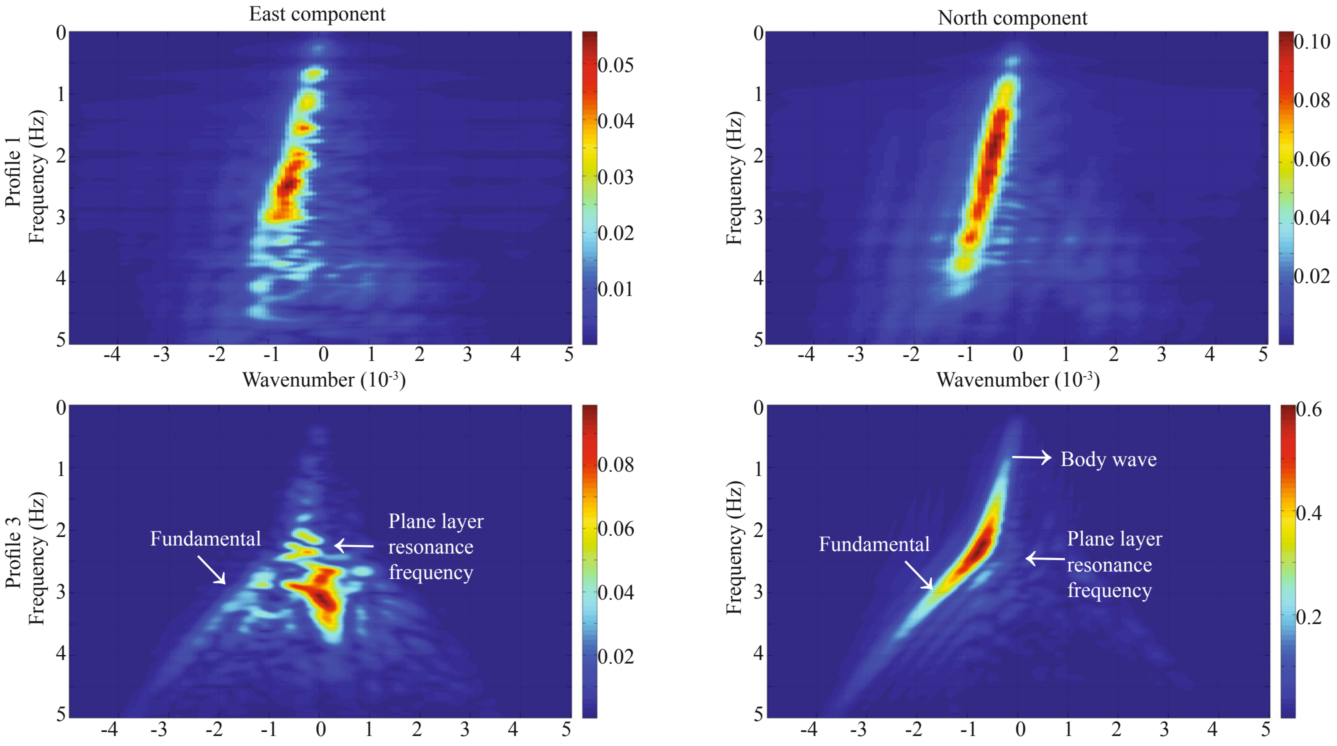

(b) Model 3

Fig. 9 Continued

velocity is 500 m/s, and as discussed above, the first two plane layer resonance frequencies become about 1.1 Hz and 3.3 Hz. On the east component (Fig. 6, Profile 3, left), the fundamental and the first higher Rayleigh modes are excited simultaneously as soon as the frequency exceeds the fundamental plane layer resonance frequency (about 1.1 Hz). On the north component (Fig. 6, Profile 3, right), the fundamental and the first higher Love modes are excited when the frequency exceeds the corresponding plane layer resonance frequencies. For Model 3, since the incident frequency does not exceed the excitation frequency of the higher mode surface wave, both at the east and the north components, only the fundamental Rayleigh and Love modes are excited as soon as the frequency exceeds the fundamental plane layer resonance frequency. These results imply that for a given incident wave, the higher mode surface waves are easier to be excited for high impedance contrast models, resulting in more complex strong motions.

The responses of Profile 1 for Models 1 and 3 in the frequency domain are shown as Fig. 9. For Model 1 (Fig. 9(a), top), the resonance phenomena in the Bowls A and B still exist for the east and north components, and the resonance frequencies of them reduce to about 0.96 Hz and 0.7 Hz, respectively, because of the lower velocity of Model 1. For Model 3 (Fig. 9(b), top), however, there is only a branch starting from the origin and with a slope equal to the shear wave velocity of the bedrock, implying that almost no surface waves are generated here and the resonance phenomenon of the Bowls A and B on Profile 1 disappeared.

Figures 10 and 11 show the PGV and E_k distributions in the basin of Models 1 and 3. For Model 1 (Fig. 10), except for the vertical component, the east and north component PGV values become smaller generally compared with the basic model, and their distributions are more localized with the north component strong ground motions concentrated in a more narrow belt zone along the western basin edge. Large E_k values are focused at the northeast and northwest basin edges and the bowls. The largest E_k value of model 1 appears around the point (20.5 km, 9.0 km), although the soil depth is only about 27 m in this area. Further analysis shows that resonance may occur here for the north component (Fig. 12), but the peak frequency of the simulated seismograms agrees well with the fundamental vertical resonance frequency value (about 1.85 Hz). For the Model 3 (Fig. 11), the distributions of the PGV and E_k are relatively smooth compared with the basic model, and the amplitudes obviously decrease. The influence of the south local bowls on the basin ground motions become less apparent and disappears for the E_k distribution, and most of the seismic energy is trapped around the corner at (18 km, 16 km).

6.2 Comparison of simulated results with the Longling earthquake damage

The basic characteristic of the simulated results are compared with the isoseismal map of the 1976 Longling earthquake (Yuan *et al.*, 1992), because this scenario earthquake and the Longling earthquake are both located

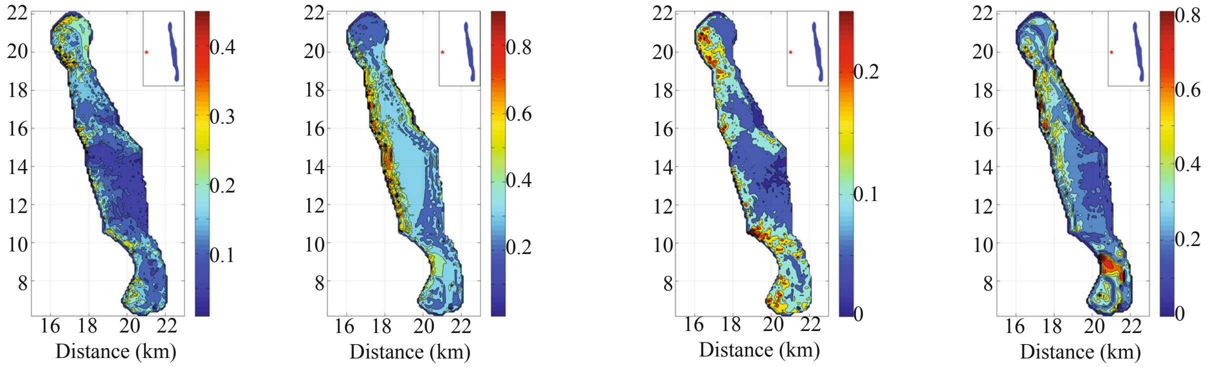

(a) (b) (c) (d)

Fig. 10 Same as Fig. 7, except for Model 1

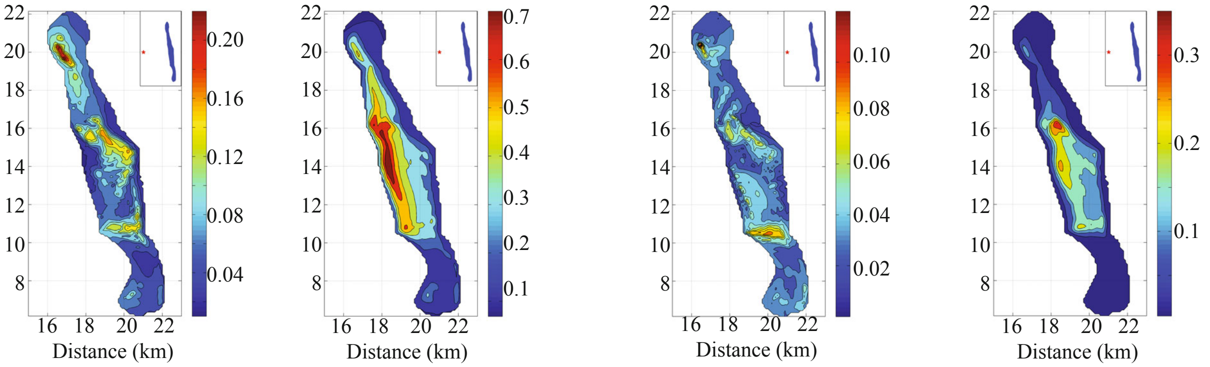

(a) (b) (c) (d)

Fig. 11 Same as Fig. 7, except for Model 3

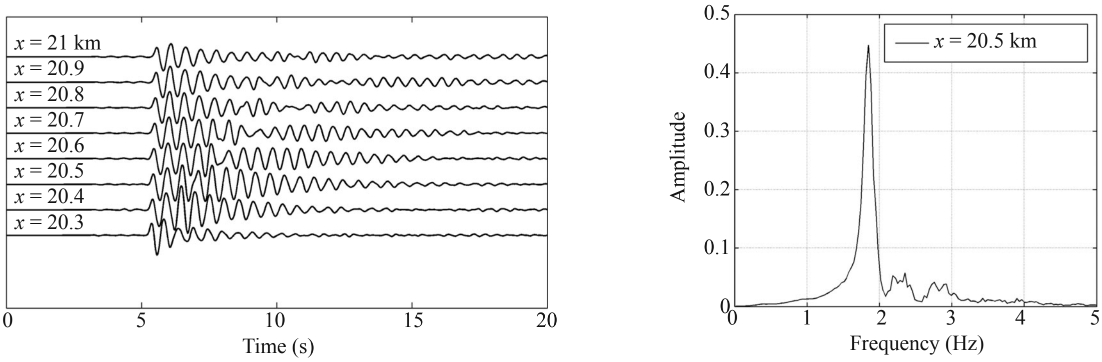

Fig. 12 North component velocity seismograms of some stations along y = 9.25 km (left) and the frequency response of site (20.5, 9.25) km (right)

at the west of the basin. In the Longling earthquake, the high anomalous intensity of VI-VIII is observed in the Shidian basin, in contrast to V in the basin surrounding region and VII near the epicenter (Fig. 1(b), according to the Chinese Intensity Table). In the Shidian basin, the largest intensity (VIII) is near the west basin edge and decreases to VI at the east basin edge. The field survey also shows that the house damage is more severe in the west part of the basin than in the east part. The damage in the area within about 100 m from the west basin boundary is slight, and the most serious damage took place in the segment about 100 m to 500 m from the boundary where some of the houses collapsed during the earthquake.

For all the models tested in this simulation, the results show that strong motions at the western basin edge are obviously stronger than at the eastern edge, and the largest amplitudes appear at regions some distance away from the west basin boundary, where the constructive interference take place between the large amplitude surface waves and the direct body waves. In addition, both the PGV and E_k distributions display a narrow belt with large values in the west basin edge. These results agree with the isoseismal map of the

Longling earthquake to some extent. The intensity map of the Shidian basin is more similar to the E_k distribution of Model 1 (Fig. 10, right). Since most of the residential houses were one or two story wood-frame structures in the basin area, which are very ductile, the cumulative damage might be a main damage type for these houses (Yuan *et al.*, 1992). It also indicates that the cumulative kinetic energy may be a better parameter to describe the damage to wood-frame structures in the basin.

7 Conclusions

In this study, the spectral element method and parallel computation technique are used to investigate the wave propagation behavior of the long and narrow Shidian basin. The 3-D basin resonance behavior, the surface wave characteristics of different geometrical profiles, and the distributions of PGV and E_k that related to the basin geometry and impedance contrast are investigated. The following basic conclusions from the analyses can be reached.

(1) In a 3D basin, when the frequency of the incident wave exceeds the fundamental resonance frequency of the equivalent plane layer ($v/4h$), the fundamental and the first higher Rayleigh modes and the fundamental Love mode can be simultaneously excited. Higher mode surface waves will be excited when the incident frequency exceeds the first higher vertical resonance frequency ($3v/4h$). This is consistent with the findings of Bard and Bouchon (1980a, b) obtained from a 2D model, suggesting that the excitation of surface wave modes in a 3D basin is similar to that of a 2D basin. However, amplitudes of different surface wave modes may depend on the location and the impedance contrast between the sediment and bedrock.

(2) Small bowls in the basin can significantly amplify the ground motions within them because of the lateral resonance when the wavelength of the lateral surface waves is comparable to the bowl width. For the 3D basin model, the multi-dimensional resonance may occur if the surface waves propagating in different directions meet and interfere constructively, which further amplify the basin ground motions.

(3) The basin amplification effect is not only determined by the sediment thickness and its velocity, but also depends on the incident direction, the source radiation pattern, the geometry of the 3D basin and the impedance contrast, etc. First, the basin-edge effect is stronger at the basin edge close to the source. For the current model, an obviously large PGV belt can be seen on the north component at the western basin edge due to its higher dip angle and the eastward incident direction, like the observations in the Kobe basin during the 1995 Kobe earthquake (Kawase, 1996). In addition, the basin-edge effect exists in all three models, particularly for the north component velocity and the cumulative kinetic energy. Second, as shown in the PGV and E_k distribution, the basin amplification effect is obviously influenced by the radiation pattern. Third, the basin ground motions near basin-internal scarps or corners may be greatly amplified or prolonged due to interference of waves from different directions. Fourth, the sediment-bedrock impedance contrast can also greatly influence the basin amplification behaviors. For high impedance contrast models, more surface wave modes can be generated, resulting in more complex time histories and PGV and E_k distributions, as well as longer shaking times. For low impedance contrast cases, the strong ground motion distributions are quite smooth, where the lateral resonance disappears and the E_k values become obviously smaller.

(4) The E_k distribution can better describe the basin effect when compared with the PGV. The agreement between the E_k distribution of Model 1 and the isoseismal map of the Longling earthquake may be a validation.

Acknowledgement

The authors would like to express their appreciation to Professor Xiong Jianguo for detailed and critical reviews. We also thank two anonymous reviewers for their constructive comments to improve the manuscript. This research is supported by the National Natural Science Foundation of China under Grant No. 51078337, No. 51108431 and No. 91315301.

References

Anderson JG, Bodin P, Brune JN, *et al.* (1986), “Strong Ground Motion from the Michoacan, Mexico, Earthquake,” *Science*, **233**(4768): 1043–1049.

Bao H, Bielak, J, Ghattas O, *et al.* (1998), “Large-scale Simulation of Elastic Wave Propagation in Heterogeneous Media on Parallel Computers,” *Comput. Methods Appl. Mech. Engrg*., **152**: 85–102.

Bard PY and Bouchon M (1980a), “The Seismic Response of Sediment-filled Valleys. Part 1. The Case of Incident SH Waves,” *Bull. Seism. Soc. Am.*, **70**(4): 1263– 1286.

Bard PY and Bouchon M (1980b), “The Seismic Response of Sediment-filled Valleys. Part 2. The Case of Incident P and SV Waves,” *Bull. Seism. Soc. Am.*, **70**(5): 1921–1941.

Chen, KC (2003), “Strong Ground Motion and Damage in the Taipei Basin from the Moho Reflected Seismic Waves during the March 31, 2002, Hualien, Taiwan Earthquake,” *Geophys. Res. Lett.*, **30**: 1151–1154.

Clayton R and Engquist B (1977), “Absorbing Boundary Conditions for Acoustic and Elastic Wave Equations,” *Bull. Seism. Soc. Am.*, **67:** 1529–1540.

Delavaud E, Cupillard P, Festa G, *et al.* (2006), “3D Spectral Element Method Simulations of the Seismic Response in the Caracas Basin,” *Third International*

Symposium on the Effects of Surface Geology on Seismic Motion, Grenoble, France, pp. 1–8.

Graves RW, Pitarka A and Somerville PG (1998), “Ground-motion Amplification in the Santa Monica Area: Effects of Shallow Basin-edge Structure,” *Bull. Seism. Soc. Am.*, **88**(5): 1224–1242.

Haskell N (1960), “Crustal Reflection of Plane SH waves,” *J. Geophys. Res.*, **65**(12): 4147–4150.

Horike M, Uebayashi H and Takeuchi Y (1990), “Seismic Response in Three-dimensional Sedimentary Basin due to Plane S Wave Incidence,” *J. Phys. Earth*, **38**: 261–284.

Kawase H (1996), “The Cause of the Damage Belt in Kobe: ‘The Basin-edge Effect,’ Constructive Interference of the Direct S-Wave with the Basin-Induced Diffracted/Rayleigh Waves,” *Seismological Research Letters*, **67**(5): 25–34.

Kim MK, Lee JS and Kim MK (2003), “Two-Dimensional Seismic Response Analysis of Basin Effects,” *KSCE Journal of Civil Engineering*, **7(1):** 33–39.

Komatitsch D, Liu QY, Tromp J, *et al.* (2004), “Simulations of Ground Motion in the Los Angeles Basin Based upon the Spectral-element Method,” *Bull. Seism. Soc. Am.*, **94**(1): 187–206.

Lee J (2013), “Earthquake Site Effect Modeling in the Granada Basin Using a 3-D Indirect Boundary Element Method,” *Physics and Chemistry of the Earth*, **63**: 102–115.

Lee SJ, Chen HW and Huang BS (2008a), “Simulations of Strong Ground Motion and 3D Amplification Effect in the Taipei Basin by Using a Composite Grid Finite-Difference Method,” *Bull. Seism. Soc. Am.*, **98**(3): 1229–1242.

Lee SJ, Chen HW, Liu QY, *et al.* (2008b), “Three-dimensional Simulations of Seismic-wave Propagation in the Taipei Basin with Realistic Topography Based upon the Spectral-element Method,” *Bull. Seism. Soc. Am.*, **98**(1): 253–264.

Liao, WI (2011),”Dynamic Responses of a Sediment-filled Valley with a Fluid Layer Subject to Incident Waves,” *Earthquake Engineering and Engineering Vibration*, **10**(2): 175–185.

Liu QF, Li XQ and Sun PS (2013), ”Study on the 3-D Velocity Model of Shidian Basin,” *Journal of Earthquake Engineering and Engineering Vibration*, **33**(3): 88–96. (in Chinese)

Olsen KB (2000), “Site Amplification in the Los Angeles Basin from Three-dimensional Modeling of Ground Motion,” *Bull. Seism. Soc. Am.*, **90**(6B): S77–S94.

Olsen KB and Schuster GT (1995), “Causes of Low-frequency Ground Motion Amplification in the Salt Lake Basin: the Case of the Vertically Incident *P* Wave,” *Geophys. J. Int.*, **122**: 1045–1061.

Paudyal YR, Yatabe R, Bhandary NP, *et al*. (2012), “A Study of Local Amplification Effect of Soil Layers on Ground Motion in the Kathmandu Valley using Microtremor Analysis,” *Earthquake Engineering and Engineering Vibration*, **11**(2): 257–268.

Pilz M, Parolai S, Stupazzini M, *et al*. (2011), “Modelling Basin Effects on Earthquake Ground Motion in the Santiago de Chile basin by a Spectral Element Code,” *Geophys. J. Int.*, **187:** 929–945.

Pitarka A, Irikura K, Iwata T, *et al.* (1998), “Three-dimensional Simulation of the Near-fault Ground Motion for the 1995 Hyogo-Ken Nanbu (Kobe), Japan, Earthquake,” *Bull. Seism. Soc. Am.*, **88**(2): 428–440.

Semblat JF, Dangla P and Kham M (2002), “Seismic Site Effects for Shallow and Deep Alluvial Basins: In-Depth Motion and Focusing Effect,” *Soil Dynamics and Earthquake Engineering*, **22:** 849–854.

Wang CY, Mooney WD, Wang XL, *et al.* (2002), “Study on 3-D Velocity Structure of Crust and Upper Mantle in Sichuan-Yunnan Region,” *Acta Seismologica Sinica*, **24**(1):1–16. (in Chinese)

Yuan YF, Yang BP and Huang SD (1992), “Damage Distribution and Estimation of Ground Motion in Shidian (China) Basin,” *Proceedings of the International Symposium on the Effects of Surface Geology on Seismic Motion*, Vol. I, Odawara, Japan, pp. 281–286.

Zhang N, Gao YF, Yang J, *et al*. (2015), “An Analytical Solution to the Scattering of Cylindrical SH Waves by a Partially Filled Semi-circular Alluvial Valley: Near-source Site Effects,” *Earthquake Engineering and Engineering Vibration*, **14**(2): 189–201.